

See discussions, stats, and author profiles for this publication at: <https://www.researchgate.net/publication/288603003>

Linear source approximation in CASMO5

Conference Paper · January 2012

CITATIONS

5

READS

28

3 authors, including:



[Rodolfo M. Ferrer](#)

Studsvik Scandpower

38 PUBLICATIONS 66 CITATIONS

[SEE PROFILE](#)



[Joel Rhodes](#)

Studsvik Scandpower

21 PUBLICATIONS 104 CITATIONS

[SEE PROFILE](#)

LINEAR SOURCE APPROXIMATION IN CASMO5

Rodolfo Ferrer and Joel Rhodes

Studsvik Scandpower, Inc.

504 Shoup Ave., Suite 201, Idaho Falls, ID 83402

rodolfo.ferrer@studsvik.com; joel.rhodes@studsvik.com

Kord Smith

Department of Nuclear Science and Engineering

Massachusetts Institute of Technology

77 Massachusetts Avenue, Cambridge, MA 02139

kord@mit.edu

ABSTRACT

A Linear Source (LS) approximation has been implemented in the two-dimensional Method of Characteristics (MOC) transport solver in a prototype version of CASMO5. The LS approximation, which relies on the computation of trajectory-based spatial moments over source regions to obtain the linear source expansion coefficients, improves the solution accuracy relative to the ‘flat’ or constant source approximation. In addition, the LS formulation is capable of treating arbitrarily-shaped source regions and is compatible with standard Coarse-Mesh Finite Difference (CMFD) acceleration. Numerical tests presented in this paper for the C5G7 MOX benchmark show that, for comparable accuracy with respect to the reference solution, the LS approximation can reduce the run time by a factor of four and the memory requirements by a factor of ten relative to the FS scheme.

Key Words: Linear source, MOC, deterministic transport, CASMO.

1. INTRODUCTION

The current transport solver implemented in Studsvik Scandpower’s CASMO5 [1] lattice physics code is based on the standard ‘flat source’ (FS) approximation widely used in the Method of Characteristics (MOC) [2, 3] scheme. In combination with Coarse-Mesh Finite Difference (CMFD) acceleration [4], the FS MOC approach has proven to be a fast and accurate solution scheme for two-dimensional transport problems. However, problems involving optically large regions with a significant degree of scattering require a large number of FS regions in order to capture the spatially-varying flux shape. Hence, there is an incentive to develop higher-order spatial approximations in order to improve the accuracy of the FS approximation.

Various schemes have been developed in order to improve the accuracy of the FS approximation, such as using the P_1 approximation to obtain an estimate of the source slope [5, 6], the linear surface characteristics schemes [7, 8], the simplified linear characteristic scheme [9], linear source approximations based on finite-difference-like slope-averaging [10, 11], and high-order diamond differencing along characteristics [12]. The Linear Source (LS) approximation presented in this work, related to the general high-order MOC scheme [13], relies on the

computation of trajectory-based spatial moments over source regions to obtain the linear source expansion coefficients. Previous work in the LS scheme includes testing in three-dimensional geometry [14] and an analysis of piece-wise linear finite-element source representation in optically thick diffusive regimes [15].

The LS approximation presented in this paper is shown to be capable of treating arbitrarily shaped source regions and is compatible with CMFD acceleration. Numerical testing for the C5G7 MOX benchmark shows that, for comparable accuracy, the LS approximation can reduce the run time by a factor of four and memory requirements by a factor of ten, relative to the FS scheme.

2. THEORY

The starting point for the LS MOC methodology is the differential form of the transport equation along a distance s_m in the azimuthal direction a and polar direction p , denoted by the double index $m = (a, p)$, of a track k located within a cell region i

$$\frac{d\psi_{m,k,i}^g}{ds_m} + \Sigma_{T,i}^g \psi_{m,k,i}^g = q_{m,k,i}^g(s_m) \quad (1)$$

where $\psi_{m,k,i}^g$ and $q_{m,k,i}^g$ correspond to the angular flux and total isotropic source (fixed plus scattering source), respectively, and $\Sigma_{T,i}^g$ denotes the transport-corrected total cross-section for energy group g . The source along the track distance is given by the following expression

$$q_{m,k,i}^g(s_m) = q_{a,k,i}^{g,0} + q_{m,i}^{g,1}(s_m - s_{m,k,i}^c) \quad (2)$$

where $s_{m,k,i}^c = s_{m,k,i} / 2$, $s_{m,k,i} = \bar{\tau}_{a,k,i} / \sin \theta_p$, and $\bar{\tau}_{a,k,i}$ is the track length in the azimuthal direction (note that $0 \leq s_m \leq s_{m,k,i}$). The inversion of the streaming-plus-collision operator on the left-hand side of Eq. (1), assuming the source along the track distance given by Eq. (2), yields the characteristics solution

$$\psi_{m,k,i}^g(s_m) = \psi_{m,k,i}^g(0) + \left(\frac{q_{a,k,i}^{g,0}}{\Sigma_{T,i}^g} - \psi_{m,k,i}^g(0) \right) E_1(\varepsilon_{m,i}^g) + \frac{q_{m,i}^{g,1}}{2(\Sigma_{T,i}^g)^2} E_3(\varepsilon_{m,i}^g) \quad (3)$$

where $\varepsilon_{m,i}^g = \Sigma_{T,i}^g s_m$ is the optical distance and $\psi_{m,k,i}^g(0)$ denotes the incoming angular flux.

The integration of the source along the characteristic yields the following expressions shown in Eq. (3)

$$E_1(\varepsilon_{m,i}^g) = 1 - e^{-\varepsilon_{m,i}^g} \quad (4)$$

and

$$E_3(\varepsilon_{m,i}^g) = 2 \left[\varepsilon_{m,i}^g - E_1(\varepsilon_{m,i}^g) \right] - \varepsilon_{m,k,i}^g E_1(\varepsilon_{m,i}^g) \quad (5)$$

where $\varepsilon_{m,k,i}^g = \Sigma_{T,i}^g s_{m,k,i}$ is constant. In the FS approximation, Eq. (4) is efficiently evaluated during the transport sweep by linearly interpolating an approximate value from pre-computed tabulated values as a function of optical length. In a similar fashion, Eq. (5) can be tabulated as functions of optical length and stored for use during the transport sweep.

The outgoing angular flux along a track length is obtained by evaluating Eq. (3) at $s_m = s_{m,k,i}$ and the balance equation is obtained by integrating Eq. (1) over the track length

$$\frac{\left[\psi_{m,k,i}^g(s_{m,k,i}) - \psi_{m,k,i}^g(0) \right]}{s_{m,k,i}} + \Sigma_{T,i}^g \Psi_{m,k,i}^{g,0} = q_{a,k,i}^{g,0} \quad (6)$$

The average angular flux over each track length, obtained from the balance equation Eq. (6), is defined as follows

$$\Psi_{m,k,i}^{g,0} \equiv \frac{1}{s_{m,k,i}} \int_0^{s_{m,k,i}} \psi_{m,k,i}^g(s_m) ds_m \quad (7)$$

The first-order moment of the angular flux,

$$\Psi_{m,k,i}^{g,1} \equiv \frac{1}{s_{m,k,i}} \int_0^{s_{m,k,i}} s_m \psi_{m,k,i}^g(s_m) ds_m \quad (8)$$

is obtained by taking the first-order moment of the characteristics equation, Eq. (3)

$$\Psi_{m,k,i}^{g,1} = \psi_{m,k,i}^g(0) s_{m,k,i}^c + \left(\frac{q_{a,k,i}^{g,0}}{\Sigma_{T,i}^g} - \psi_{m,k,i}^g(0) \right) \frac{\Gamma_1(\varepsilon_{m,k,i}^g)}{\Sigma_{T,i}^g} + \frac{q_{m,i}^{g,1}}{2(\Sigma_{T,i}^g)^2} s_{m,k,i} \Gamma_3(\varepsilon_{m,k,i}^g) \quad (9)$$

where

$$\Gamma_1(\varepsilon_{m,k,i}^g) = 1 + \frac{\varepsilon_{m,k,i}^g}{2} - \left(1 + \frac{1}{\varepsilon_{m,k,i}^g} \right) E_1(\varepsilon_{m,k,i}^g) \quad (10)$$

$$\Gamma_3(\varepsilon_{m,k,i}^g) = \frac{\varepsilon_{m,k,i}^g}{6} - \frac{2}{\varepsilon_{m,k,i}^g} - 2 + \left(1 + \frac{1}{\varepsilon_{m,k,i}^g} \right) \left(1 + \frac{2}{\varepsilon_{m,k,i}^g} \right) E_1(\varepsilon_{m,k,i}^g) \quad (11)$$

In cases where the medium is optically thin, i.e. $\varepsilon_{m,k,i}^g \rightarrow 0$, a set of approximations are used in order to avoid numerical round off error. In particular, a Taylor series is expanded about $\varepsilon_{m,k,i}^g = 0$ and truncated after the first few terms.

The scalar flux over the cell is expanded into a linear function

$$\phi_i^g(x, y) = \phi_{i,c}^g + \phi_{i,x}^g x + \phi_{i,y}^g y \quad (12)$$

where the local coordinates, defined as $x = X - X_i^c$ and $y = Y - Y_i^c$, are centered at (X_i^c, Y_i^c) with respect to the global coordinate system (X, Y) . These are the coordinates of the pre-computed ‘numerical centroid’ using the tracking information for each source region. In order to obtain the expansion coefficients $\{\phi_{i,c}^g, \phi_{i,x}^g, \phi_{i,y}^g\}$, a cell-wise 3×3 matrix is defined whose elements represent the spatial moments of the scalar flux expansion, given by Eq. (12).

In general, given f and g , the integration of these two functions is numerically evaluated using the tracking information via the following expression

$$\frac{1}{V_i} \int_{V_i} f(x, y) g(x, y) dV = \frac{1}{V_i} \sum_m \omega_m \delta A_a \sum_k \left[\int_0^{s_{m,k,i}} f(s_m) g(s_m) ds_m \right] \quad (13)$$

where $\omega_m = \omega_p \sin \theta_p \omega_a$ are the weights associated with m^{th} direction of a product quadrature, δA_a is the width of the characteristic, and f and g are integrated along the track k . The track lengths used to evaluate the trajectory-based integration over the cell regions differ slightly from the tracks generated by the geometry ray tracing routine due to a renormalization which conserves the region volume. The region-wise normalization factor relates the two track quantities such that $s_m = \xi_i t_m$, where t_m is the ‘geometrical’ track length. Hence, assuming $f = g = 1$, the numerical integration shown in Eq. (13) is equal to unity.

The coordinates for the ‘numerical centroid’ are defined as follows

$$X_i^c = \frac{1}{V_i} \sum_m \omega_m \delta A_a \sum_k \left[\int_0^{s_{m,k,i}} X(s_m) ds_m \right] \quad (14)$$

$$Y_i^c = \frac{1}{V_i} \sum_m \omega_m \delta A_a \sum_k \left[\int_0^{s_{m,k,i}} Y(s_m) ds_m \right] \quad (15)$$

Since the local coordinate system is centered about these centroids, the average scalar flux is exactly equal to the constant expansion term in Eq. (12), i.e.

$$\phi_{i,c}^g = \frac{1}{V} \int_V \phi_i^g(x, y) dV \quad (16)$$

Consequently, the cell-wise linear system is reduced to a 2×2 matrix whose elements are given by the following equations

$$M_{xx} = \frac{1}{V_i} \sum_m \omega_m \delta A_a \sum_k \left[\int_0^{s_{m,k,i}} (x(s_m))^2 ds_m \right] \quad (17)$$

$$M_{yy} = \frac{1}{V_i} \sum_m \omega_m \delta A_a \sum_k \left[\int_0^{s_{m,k,i}} (y(s_m))^2 ds_m \right] \quad (18)$$

$$M_{xy} = \frac{1}{V_i} \sum_m \omega_m \delta A_a \sum_k \left[\int_0^{s_{m,k,i}} x(s_m) y(s_m) ds_m \right] \quad (19)$$

The numerical centroids and moments, Eqs. (14)-(15) and (17)-(19) respectively, are independent of energy group and material composition, and may be pre-computed and stored for later use to obtain the expansion coefficients of the linear source.

The average and first-order moments of the angular flux over each track length must be related to the scalar flux spatial moments in order to obtain the expansion coefficients in Eq. (12).

Recalling the definitions of the average and first-order moment of the angular flux, Eqs. (7) and (8) respectively, the trajectory-based numerical moments are defined as follows

$$\phi_{i,c}^g = \frac{1}{V_i} \sum_m \omega_m \delta A_a \sum_k \Psi_{m,k,i}^{g,0} s_{m,k,i} \quad (20)$$

$$\Phi_{i,x}^g = \frac{1}{V_i} \sum_m \omega_m \delta A_a \sum_k \left(a_m^x \Psi_{m,k,i}^{g,1} / \xi_i + x_{a,k,i}^{in} \Psi_{m,k,i}^{g,0} \right) s_{m,k,i} \quad (21)$$

$$\Phi_{i,y}^g = \frac{1}{V_i} \sum_m \omega_m \delta A_a \sum_k \left(a_m^y \Psi_{m,k,i}^{g,1} / \xi_i + y_{a,k,i}^{in} \Psi_{m,k,i}^{g,0} \right) s_{m,k,i} \quad (22)$$

Finally, the cell-wise source is assumed to be isotropic, and a linear function in two-dimensional space

$$q_i^g(x, y) = q_{i,c}^g + q_{i,x}^g x + q_{i,y}^g y \quad (23)$$

The expansion coefficients in Eq. (2) may be obtained in terms of the coefficients in Eq. (23) by substituting $x(t_m) = a_m^x t_m + x_{a,k,i}^{in}$ and $y(t_m) = a_m^y t_m + y_{a,k,i}^{in}$ into the latter and solving for the coefficients

$$q_{a,k,i}^{g,0} = q_{i,c}^g + q_{i,x}^g x_{a,k,i}^c + q_{i,y}^g y_{a,k,i}^c \quad (24)$$

$$q_{m,i}^{g,1} = (q_{i,x}^g a_m^x + q_{i,y}^g a_m^y) / \xi_i \quad (25)$$

where $(x_{a,k,i}^c, y_{a,k,i}^c)$ are the coordinates of the track midpoint relative to the local coordinate system.

Given the source expansion coefficients from a guess or previous iterate, the transport sweep is performed for each angular direction to obtain the average and first-order moment of the angular flux across each track length. These angular flux quantities are used to compute the trajectory-based spatial moments of the scalar flux, which is subsequently used to obtain the scalar flux expansion coefficients. Due to the linearity of the fission and scattering operator, the source expansion coefficients are directly obtained from the scalar flux coefficients. This process is repeated, with the inclusion of acceleration, until the desired convergence criteria are satisfied.

3. NUMERICAL RESULTS

The LS MOC scheme derived in the previous section was implemented into a special “developer version” of CASMO5 for testing. In order to test the accuracy of the LS scheme and compare to FS MOC, the C5G7 MOX benchmark was selected for the testing. Since the benchmark contains large reflector regions in the periphery of the problem domain, which requires rather fine meshing to capture the flux shape, it is expected that the LS approximation will prove advantageous for this problem. Previous work [16] has shown that CASMO5 obtains very accurate solutions for the C5G7 MOX benchmark relative to the Monte Carlo reference solution.

The two-dimensional C5G7 MOX benchmark consists of four 17×17 UO_2 and MOX assemblies arranged in a colorset pattern surrounded by a water reflector region with an assembly pitch of 21.42 cm. Reflective boundary conditions are applied in the west and north boundaries and vacuum on the south and east boundaries (quarter-core symmetry). Figure 1 depicts the benchmark geometry and material composition. The UO_2 assemblies are located along the diagonal and MOX assemblies across from the diagonal.

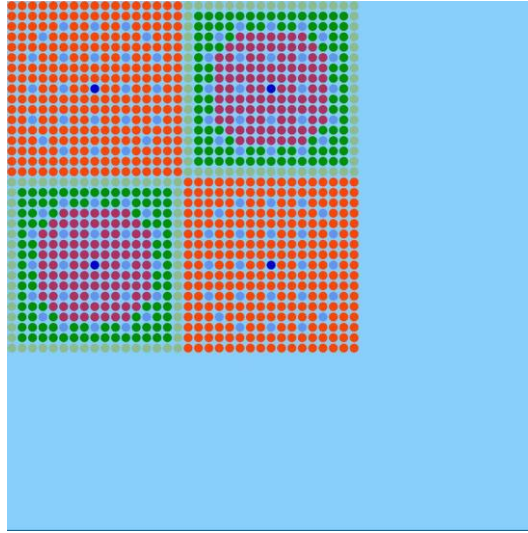


Figure 1. C5G7 MOX Benchmark geometry (generated by CASMO5).

A total of seven cases were executed involving a combination of four spatial grids and the two source representations. The four spatial grids consisted of the following: a coarse mesh throughout the whole domain, a fine mesh within the fuel region and a coarse mesh throughout the reflector, a coarse mesh within the fuel region and a fine mesh throughout the reflector, and a fine mesh throughout the whole domain.

The fine mesh within the fuel region used 5 rings (source regions) in the fuel and 10 rings in the coolant region. In addition, an azimuthal division consisting of 16 regions was applied to all pin cell regions. The fine mesh throughout the water reflector region was discretized by using a $0.1 \text{ cm} \times 0.1 \text{ cm}$ mesh. The coarse mesh case within the fuel region used no additional rings in the fuel or in the coolant region. An azimuthal division consisting of 8 regions was applied to all pin cell regions in the coarse mesh case. Finally, the coarse mesh reflector region was discretized using a $0.5 \text{ cm} \times 0.5 \text{ cm}$ mesh.

The fine mesh for the UO_2 corner assembly and neighboring water reflector region is shown below in Fig. 2 on the left. A detailed view of the pin cell mesh is shown embedded in the fine mesh schematic on the lower right corner. An analogous schematic for the coarse mesh case is shown on the right in Fig. 2.

All calculations used 128 azimuthal angles, 3 polar angles, and 0.05 cm ray spacing. The default eigenvalue and pointwise flux convergence criteria, 1 pcm and $1.0\text{E-}4$, respectively, were applied to all cases.

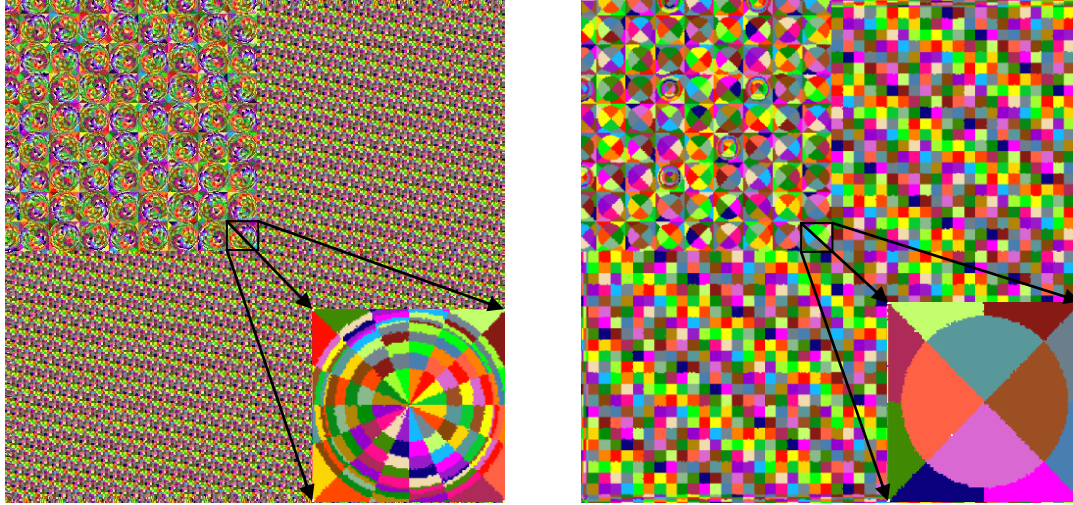


Figure 2. C5G7 MOX benchmark UO_2 /reflector region fine mesh (left) and coarse mesh (right).

A summary of the seven cases is shown in Table I based on various combinations of the spatial meshes and source representations. The goal of the case matrix is twofold: to evaluate the relative improvement in accuracy due to applying a better source representation (LS) over coarse mesh regions, and to compare the benefits of using LS on a coarse mesh and FS on fine mesh.

Table I. Case matrix used in comparisons for the C5G7 MOX benchmark (FUE=fuel, REF=reflector).

Case	Mesh (FUE/REF)	Source (FUE/REF)
1	Coarse	FS
2	Coarse	FS/LS
3	Coarse	LS/FS
4	Coarse	LS
5	Fine	FS
6	Fine/Coarse	FS/LS
7	Coarse/Fine	LS/FS

A summary of the eigenvalue error, maximum/minimum peak pin power errors, total transport iterations, relative memory requirements, and run times are shown in Table 1 below for all seven cases. All cases were executed on a 2.66 Ghz Intel Quad Core Linux PC using a single CPU, though MOC parallelization is theoretically possible.

Table II. Comparison of overall results from case matrix solutions to the C5G7 MOX benchmark.

Case	Eigenvalue Error (pcm)	Max. Power Error (%)	Min. Power Error (%)	MOC Iters.	Memory (Rel.)	MOC Run time (s)
1	56.6	-0.769	3.879	8	1	82.2
2	36.1	-0.504	2.302	8	1.01	105.9
3	16.2	-0.226	1.624	8	1.01	108.1
4	-2.9	0.024	0.298	8	1.01	121.5
5	10.2	-0.036	0.598	8	11.44	487.8
6	8.5	-0.024	0.586	8	2.01	222.0
7	-1.1	0.012	0.370	8	6.61	471.9

The first set of cases (1-4) indicates an improvement in accuracy in terms of a reduction in eigenvalue and maximum/minimum power percent error as the source representation in either the fuel or reflector region (or both) is changed from FS to LS, and the mesh remains constant. The penalty incurred by using the LS scheme is reflected in larger relative memory requirements and solver run times. The additional memory requirements in cases 2 through 4 are due to the storage of LS-related quantities.

The second set of cases (5-7) indicates an improvement in accuracy when the mesh is only refined throughout FS regions, relative to the accuracy achieved in cases 1-3. In addition, cases 6 and 7 have slightly better accuracy than case 5, which is considered the most accurate solution to the C5G7 benchmark using an FS-only approach [16].

However, the replacement of the LS scheme on a coarse grid by the FS scheme on a fine grid significantly increases the memory requirements and solver run times to achieve comparable accuracy. For example, case 6 uses twice the memory and run time required by case 4, while achieving no significant gain in accuracy. Although case 7 achieves slightly better overall accuracy than case 4, the memory and run time requirements are large relative to case 4 and comparable in magnitude to those in case 5.

For comparable accuracy, the case 4 run time is a factor of four lower than the FS run time on the fine mesh. This relative advantage is due to the fact that a large number of mesh regions must be placed in the reflector region in order to capture the scalar flux shape in the FS scheme. A consequence of this fine mesh is the larger memory required to store the track length data across many mesh regions in the reflector. Hence, the memory requirements for case 5 are roughly a factor of ten higher than case 4.

The use of CMFD acceleration for the LS scheme was found to be just as efficient, in terms of the total number of MOC iterations (transport sweeps), as in the case of the FS scheme for the

C5G7 benchmark. The compatibility and efficiency of acceleration methods for higher-order schemes, such as the LS approximation, is very important for realistic lattice calculations and large problems involving multiple fuel assemblies. The relatively short MOC run times for cases 4 and 5 (2 and 8 minutes, respectively) do not take into account the run time needed to setup the problem geometry, e.g. ray tracing, nor the time necessary to solve the low-order CMFD system of equations. The total CASMO5 run time using the LS scheme on the coarse mesh is almost nine times lower than the fine mesh FS run time.

A detailed comparison of the error distribution for the case matrix is shown in Table III below. The error distribution is assessed through the use of various metrics. In particular, the average percent error (APE) is a simple average of the error over all the pin cells, while the maximum absolute percent error (MPE) is the maximum value of the error distribution. The RMS error is similar to the APE, except it gives more weight to the higher percentage error. The mean relative error (MRE), arguably the most accurate measure of error in the pin power distribution, directly weights the percent error with the pin powers. Finally, the percentage of fuel pins which fall within a 68 % confidence interval is tabulated in the table.

The trends observed in the comparison of the overall results (Table II) may be verified by comparing the APE and MRE values for all seven cases in Table III. However, the MPE and RMS values are higher than expected for cases 3 and 7. In order to further investigate this behavior, the error distribution for cases 1 through 4 was examined and is shown in Figure 3.

Table III. Comparison of the error metrics for the case matrix solutions to the C5G7 MOX benchmark.

Case	Ave. % Error	Max. % Error	RMS Error	Mean. Rel. Error	% Fuel Pins within one S.D.
1	0.807	4.437	1.222	0.633	14.0
2	0.432	2.302	0.565	0.365	18.4
3	0.379	3.268	0.715	0.282	35.0
4	0.132	0.720	0.175	0.109	61.1
5	0.153	0.692	0.198	0.132	49.5
6	0.149	0.665	0.191	0.129	50.4
7	0.126	0.732	0.168	0.104	64.5

The distributions in Figure 3 indicate the location of the maximum error and the reduction in error as the source representation is improved from FS to LS in cases 1 through 4. The highest percent error in cases 1-3 is located along the fuel/reflector interface. A comparison of cases 2 and 3 indicates that the use of FS within the fuel and LS throughout the reflector (case 2) minimizes the maximum error relative to case 3. However, the opposite approach (case 3) will

possess a higher maximum error but a lower average percent error throughout the fuel region. A similar trade-off may be observed by plotting the error distribution for cases 5 through 7 in which case 7 possesses the largest MPE and also a low APE and MRE. This explains the MPE and RMS behavior observed in Table III for cases 3 and 7.

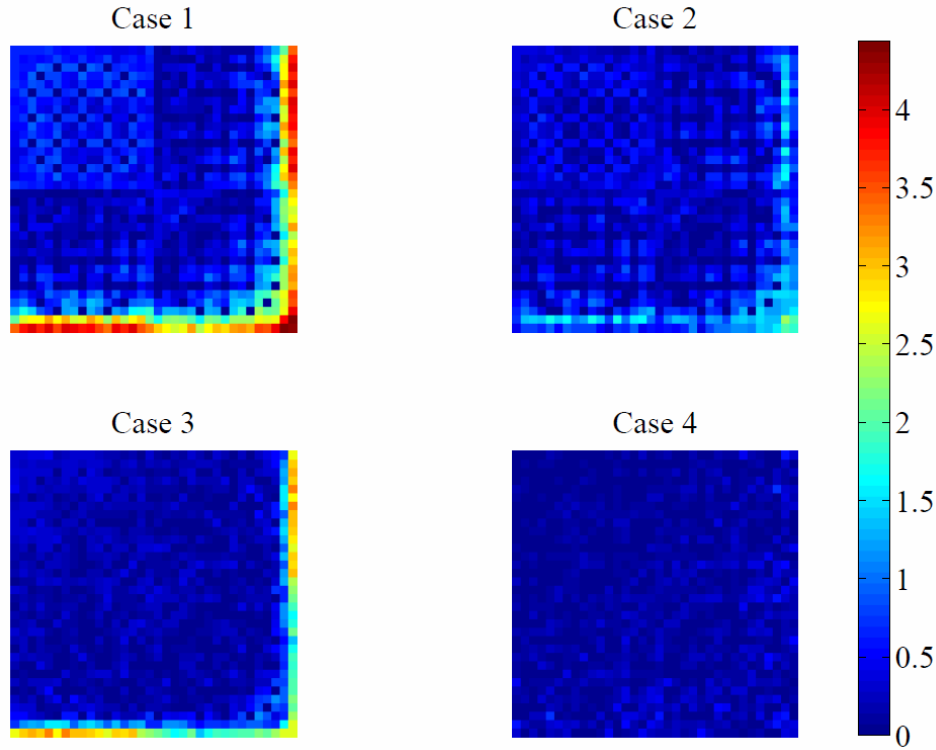


Figure 3. Fuel pin power percent error distributions for cases 1 through 4.

3. CONCLUSIONS

A Linear Source (LS) approximation has been implemented into CASMO5 which improves the accuracy and the efficiency, as measured by run time and memory requirements, relative to the Flat Source (FS) MOC scheme for a comparable level of accuracy. The LS MOC relies on trajectory-based numerical spatial moments for computation of the linear expansion coefficient for the scalar flux. Numerical results using the C5G7 MOX benchmark indicate the advantage of using the LS scheme over the FS scheme for problems with large reflector regions which require many cell regions in order to capture the spatial shape of the scalar flux. The results from numerical tests indicate an improvement in the coarse mesh LS scheme run time and memory of a factor of four and ten, respectively, relative to the fine mesh FS scheme, for a comparable level of accuracy.

REFERENCES

1. J. Rhodes, D. Lee, K. Smith, "CASMO-5/CASMO-5M A Fuel Assembly Burnup Program Methodology Manual," SSP-08/405 Rev. 0 (2008).
2. R. Askew, "A Characteristic Formulation of the Neutron Transport Equation in Complicated Geometries," AEEW-M, 1108 (1972).
3. M. J. Halsall, "CACTUS, A Characteristics Solution of the Neutron Transport Equations in Complicated Geometries," AEEW-R-1291, U.K. Atomic Energy Authority (1980).
4. K. S. Smith, J. D. Rhodes, "Full-Core, 2-D, LWR Core Calculations with CASMO-4E," *Proc. of the PHYSOR 2002*, Seoul, Korea, Oct. 7-10 (2002).
5. P. Petkov, T. Takeda, "Transport Calculations of MOX and UO₂ pin cells by the Method of Characteristics," *J. Nucl. Sci. Technol.* **35**, pp. 874-885 (1998).
6. C. Rabiti, G. Palmiotti, W. S. Yang, M. A. Smith, D. Kaushik, A. B. Wollaber, "Quasi Linear Representation Of The Isotropic Scattering Source For The Method of Characteristics," *Proc. of the M&C 2009*, Saratoga Springs, New York, May 3-7 (2009).
7. S. Santandrea, R. Sanchez, "Positive Linear and Nonlinear Surface Characteristic Schemes for the Neutron Transport Equation in Unstructured Meshes," *Proc. of the PHYSOR 2002*, Seoul, Korea, Oct. 7-10, (2002).
8. S. Santandrea, R. Sanchez, P. Mosca, "A Linear Surface Characteristics Approximation for Neutron Transport in Unstructured Meshes," *Nucl. Sci. Eng.*, **160**, pp. 23-40 (2008).
9. R. Le Tellier, A. Hébert, "On the Integration Scheme Along a Trajectory for the Characteristics Method," *Ann. of Nucl. Energy* **33**, pp. 1260-1269 (2006).
10. M. J. Halsall, "Neutron Transport in WIMS by the Characteristic Method," *Trans. Am. Nucl. Soc.* **68**, 454 (1993).
11. C. Tang, S. Zhang, "Development and Verification of an MOC code Employing Assembly Modular Ray Tracing and Efficient Acceleration Techniques," *Ann. of Nucl. Energy* **36**, pp. 1013-1020 (2009).
12. A. Hébert, "High-Order Diamond Differencing Along Finite Characteristics," *Nucl. Sci. Eng.*, **169**, pp. 81-97 (2011).
13. E. Masiello, R. Clemente, S. Santandrea, "High-Order Method of Characteristics For 2-D Unstructured Meshes," *Proc. of the M&C 2009*, Saratoga Springs, New York, May 3-7 (2009).
14. X. M. Chai, K. Wang, "The Linear Source Approximation In Three Dimension Characteristic Method," *Proc. of the M&C 2009*, Saratoga Springs, New York, May 3-7 (2009).
15. T. M. Pandya, M. L. Adams, W. Daryl Hawkins, "Long Characteristics with Piecewise Linear Sources Designed for Unstructured Grids," *Proc. of the M&C 2011*, Rio de Janeiro, RJ, Brazil, May 8-12 (2011).
16. D. J. Lee, J. Rhodes, K. Smith, "CASMO-5 Solutions for the Two-Dimensional C5G7 MOX Benchmark Problem," *Trans. Am. Nucl. Soc.* **99**, 680 (2008).